

Q-SLAM: Quadric Representations for Monocular SLAM

Chensheng Peng^{1*}, Chenfeng Xu^{1*}, Yue Wang², Mingyu Ding¹, Heng Yang²
 Masayoshi Tomizuka¹, Kurt Keutzer¹, Marco Pavone², and Wei Zhan¹

¹ UC Berkeley
² NVIDIA

Abstract. Monocular SLAM has long grappled with the challenge of accurately modeling 3D geometries. Recent advances in Neural Radiance Fields (NeRF)-based monocular SLAM have shown promise, yet these methods typically focus on novel view synthesis rather than precise 3D geometry modeling. This focus results in a significant disconnect between NeRF applications, *i.e.*, novel-view synthesis and the requirements of SLAM. We identify that the gap resulting from the volumetric representations used in NeRF, which are often dense and noisy. In this study, we propose a novel approach that reimagines volumetric representations through the lens of quadric forms. We posit that most indoor scene components can be effectively represented as quadric planes. Leveraging this assumption, we reshape the volumetric representations with million of cubes by several quadric planes, which leads to more accurate and efficient modeling of 3D scenes in SLAM contexts. Our method involves two key steps: First, we use the quadric assumption to enhance noisy depth estimations obtained from the tracking module. This step alone significantly improves depth estimation accuracy. Second, in the subsequent mapping phase, we diverge from previous NeRF-based SLAM methods that distribute sampling points across the entire volume space. Instead, we concentrate sampling points around quadric planes and aggregate them using a novel quadric-decomposed Transformer. The quadric semantics are not only explicitly used for depth correction and scene decomposition, but also serve as an implicit supervision signal during the training of NeRF network. Additionally, we introduce an end-to-end joint optimization strategy that synchronizes pose estimation with 3D reconstruction. Through rigorous experimental evaluation, our method exhibits superior performance over other approaches relying on estimated depth. Furthermore, our method achieves accuracy comparable to methods utilizing ground truth depth, marking a significant advancement in the field of monocular SLAM and the integration of NeRF-based techniques for accurate 3D geometry modeling and joint optimization of camera poses.

Keywords: Neural Radiance Fields · Simultaneous Localization and Mapping

1 Introduction

Recent years have seen a renaissance of simultaneous localization and mapping (SLAM), thanks to the advances in learning-based localization methods [36, 40, 49] and neural radiance fields (NeRFs) [22, 30, 52]. In its basic incarnation, SLAM involves estimating per-frame camera poses and reconstructing 3D scenes from visual inputs. The

key challenging of monocular SLAM lies in the accurate 3D scene geometry modeling from visual inputs.

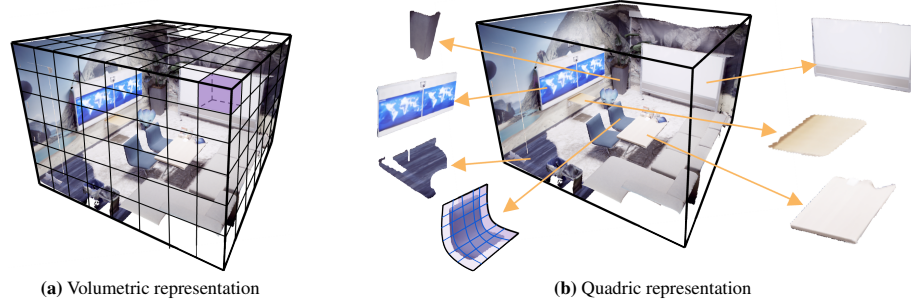


Fig. 1: Comparison between the volume representation and our quadric representation. With an off-the-shelf segmentation network, we can partition the 3D scenes into different quadric surfaces. Instead of processing every points independently, we can fully exploit the correlation between points on and across the quadric surfaces.

To enable high-quality 3D scene reconstruction, recent SLAM approaches resort to NeRFs and Gaussians as key map representations. Specifically, NeRFs [14], employing neural networks *i.e.* MLPs, are recognized for their ability to achieve photo-realistic novel-view synthesis, as demonstrated in studies such as iMAP [30], Nice-SLAM [52]. Conversely, 3D Gaussian Splatting (3DGS) [11] relies on dense Gaussian representations to learn scene geometries effectively. Despite achieving photo-realistic novel-view synthesis, NeRFs and Gaussians are not necessarily compatible in SLAM systems, with several drawbacks. On the one hand, MLP-based NeRFs are slow to train while achieving significant memory efficiency. On the other hand, 3D Gaussian Splatting offers near-real-time training capabilities but suffer from large memory consumption and sensitivity to inaccurate camera pose estimation. Additionally, both methods focus on dense high-quality reconstruction, demanding substantial representation efforts to capture fine-grained details.

Addressing these challenges necessitates the design of map representations that are compatible with both learning-based localization front-end and NeRF(GS)-based reconstruction module. Therefore, to enhance scene geometry representation in SLAM, we introduce a novel method, termed **Q-SLAM**. This approach begins with a fundamental premise: most scene elements, particularly in indoor environments, are effectively representable by quadric planes, as illustrated in Figure 1. Leveraging this assumption, we integrate the proposed quadric representations across the SLAM pipeline in several key areas.

1. The well-established front-end tracking module can take RGB stream as input and offer a rough depth estimation while estimating camera poses. Nevertheless, this depth estimation encounters significant challenges, particularly at edges and in texture-less regions, where accuracy tends to degrade. To address these issues, we

- introduce a *quadric-based depth correction* module, leveraging quadric surfaces to refine the depth estimation, thus improving overall scene reconstruction accuracy, especially in complex and challenging environments.
2. In the mapping module, departing from previous NeRF-based SLAM approaches like [22, 52], which rely on volumetric representations, our method transforms densely volumetric scenes - comprising millions of cubes (*e.g.*, $300 \times 300 \times 300$ voxels) - into a more manageable set of quadric surfaces (50-100 quadric surfaces per keyframe). This approach maintains the integrity of the 3D scene descriptions while significantly reducing complexity, by sampling around the quadric surfaces instead of the whole 3D space.
 3. During the rendering phase, we develop a *quadric-ray transformer*. We employ importance-sampling based on the quadric-rectified depth values, and we emphasize that sampled points on a quadric naturally belong to the same instance, which facilitates the modeling of their interrelationships during rendering, akin to the method in [12, 38]. We first perform feature interaction between points along a ray to aggregate information and then model the relationships between these surface points across rays using a transformer.
 4. Notably, we extend the utility of quadric semantics beyond mere depth correction and scene decomposition. They are also used as a supervision signal throughout the optimization of the NeRF network to learn robust and accurate features. With the integration of quadrics into the pipeline, we also consider the estimated pose as a learnable parameter in our mapping phase. This introduces a differentiable optimization process to refine the pose estimation, enhancing overall system accuracy and efficiency.

We conduct experiments on Replica [28], ScanNet [6], and TUM RGB-D [29], and evaluate the results on novel-view synthesis, depth estimation, and pose estimation tasks. The results demonstrate the effectiveness of Q-SLAM, with 6.9 % PSNR (for novel-view synthesis) and 13.2 % L1 error (for depth estimation) improvements on Replica dataset, 4.1 %, 5.7 % ATE (for pose estimation) improvements on ScanNet, and TUM RGB-D datasets, respectively.

2 Related Work

2.1 Dense Visual SLAM

Neural Radiance Fields (NeRF) [13] have exhibited notable efficacy in diverse applications, including view synthesis [13, 37, 38] and 3D reconstruction [2, 4]. Concurrently, Simultaneous Localization and Mapping (SLAM) confronts the challenge of precisely determining the pose of a moving sensor within an environment. The output pose of SLAM aligns seamlessly with the input requirements of NeRF, making NeRF a natural choice as the mapping backbone in a SLAM system. **RGBD SLAM:** Innovative contributions such as iMAP [30] and Nice-SLAM [52] have pioneered the integration of NeRF into SLAM systems, demonstrating commendable tracking and mapping performance for indoor scenes. Co-SLAM [36] adopts a multi-resolution hash-grid representation for the scene to expedite convergence. E-SLAM [9] integrates the

multi-scale axis-aligned perpendicular feature planes for efficient reconstruction of 3D scenes. By anchoring neural scene features in a point cloud generated iteratively in an input-driven manner, Point-SLAM [25] optimizes runtime and memory usage while maintaining fine detail resolution. Besides using NeRF as the map representation, recent SLAM systems also resort to 3D Gaussian Splatting (3DGS) [11] due to its explicit representation property and real-time rendering performance. SplaTAM [10] pioneers in replacing NeRF with 3DGS and has achieved promising results in both tracking and mapping. GS-SLAM [43] further proposes a coarse-to-fine technique to select reliable 3D Gaussian representations for camera pose optimization effectively. However, these GS-based approaches have one drawbacks in common, much higher requirements for memory usage.

All these approaches above rely on ground truth depth map for supervision of NeRF (or 3DGS) training, which is hard to obtain in real-world environment, thereby limiting their applicability in robotics. Conversely, **Monocular SLAM** method emerges, with only RGB images as input. In particular, Nerf-SLAM [22] integrates DROID-SLAM [34] for pose estimation and depth prediction and use Instant-NGP [16] to fit a NeRF. GO-SLAM [49] globally optimize poses and 3D reconstruction. However, the performance of these methods in 3D reconstruction is impeded by the inherent limitations of noisy predicted depth maps.

2.2 Scene representations

Volumetric Representations are predominantly utilized in Neural Radiance Fields (NeRFs) [3, 13, 17], and in the 3D perception field [21, 23, 41]. These representations encapsulate a 3D scene through a volumetric approach, where each volume element embodies occupancy probabilities or task-specific features. However, deriving volumetric representations solely from visual inputs presents significant challenges, particularly in terms of geometric estimation, leading to ambiguous and noisy outputs. **Point-Cloud Representation** offers a sparser alternative [42]. Point-SLAM [25] utilize a dynamic point density strategy to reduce computational and memory usage. Yet sparse point-clouds struggle to depict scenes comprehensively, while dense point-clouds encounter similar complications to volumetric representations, as previously mentioned. Consequently, few vision-based SLAM systems adopt point-based representations. Additionally, primitives like **Planes** [7] and **Quadric-Meshes** [8, 15, 31] have been proposed for scene representation. QuadricSLAM [20] estimates 3D quadric surfaces from 2D multi-view images and uses them as landmark representations for camera tracking in the SLAM pipeline. Dense Planar SLAM [24] uses bounded planes and surfels extracted from depth images to build a real-time SLAM system, but ignore the fine-grained reconstruction of 3D scenes. Point-plane SLAM [48] exploits the constraints of plane edges, which are predominant features that are less affected by measurement noise. ManhattanSLAM [45] utilizes the indoor structural information to estimate camera poses based on the Manhattan World (MW) assumption. However, these are typically employed for regularization during optimization or are challenging to optimize due to the need to train parameters from scratch, limiting their applicability in visual SLAM.

Drawing inspiration from **quadric representations** in LiDAR SLAM [40], we introduce quadric representations in visual monocular SLAM. Instead of merely using

quadric primitives for regularization, we integrate them comprehensively into the entire SLAM pipeline, including depth correction, the innovative quadric ray transformer and the quadric semantics as supervision signal.

3 Q-SLAM

3.1 Overview

Our framework, Q-SLAM, as illustrated in Fig. 2, takes monocular RGB sequences as input. Initially, the tracking module predicts rough depth maps and initial camera poses from these inputs. Concurrently, a pretrained segmentation network is employed to estimate segmentation masks from these images. These masks are then utilized by the quadric-based depth correction module to refine the noisy depth maps, yielding more accurate corrected depth maps. Alongside the corresponding RGB images, camera poses, and segmentation results, they are inputted into the Neural Radiance Fields (NeRF) network [13].

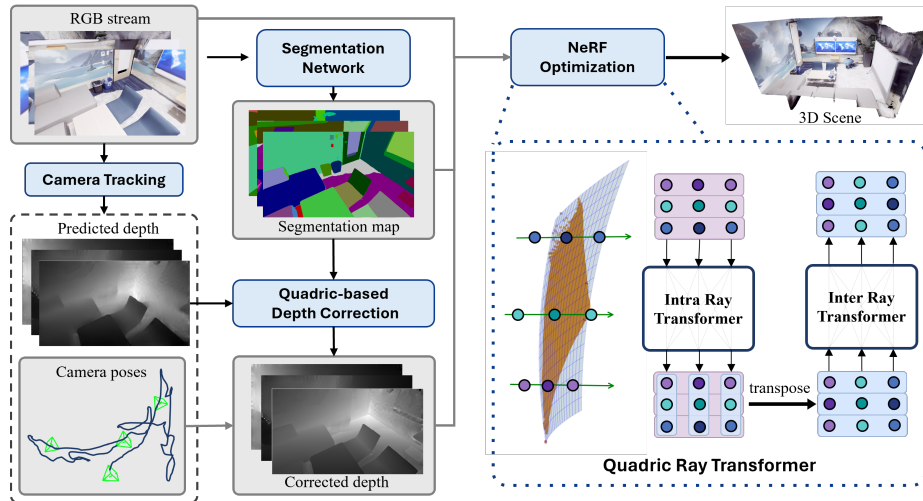


Fig. 2: Overview of our proposed method. From the input RGB sequences, depth map, camera pose and segmentation mask can be predicted. Subsequently, the initially estimated depth undergoes correction based on the quadric assumption. Along with the segmentation mask, camera poses, and image frames, the corrected depth are used for optimization of NeRF network. During the 3D reconstruction process, our proposed quadric ray transformer leverages the quadric priors effectively.

For NeRF optimization, the RGB images, corrected depth and segmentation masks serve as supervision signals. To capture the semantic relationship across quadric surfaces, we further propose a quadric ray transformer, enabling effective feature interaction within and across the sampled rays. During the mapping process, both the camera

poses $\mathbf{G} = g_t$ and the 3D scene representation parameters Θ are jointly optimized to enhance tracking and mapping accuracy. With the learned NeRF parameters, we can render RGB images, depth maps, and semantic maps for novel views, which can then be utilized to reconstruct the 3D mesh using TSDF-Fusion [46].

3.2 Quadric depth correction

Quadric surface fitting We introduce quadric representations for scene components. First, each point is classified by a segmentation network. Using the segmentation mask, we can crop out all the segmented patches in a frame, forming a set of depth patches. Afterward, the depth patches will be projected into 3D spaces with the given calibration matrix. Our proposed quadric fitting is applied to the patches.

To represent the segmented points as quadric surfaces, we define the quadric implicit function as

$$f(\mathcal{C}, \mathbf{x}) = \mathcal{C}_q^T \mathbf{q} + \mathcal{C}_l^T \mathbf{x} = c \quad (1)$$

where $\mathbf{x} = [x, y, z]^T$ is the linear term and $\mathbf{q} = [x^2, y^2, z^2, xy, yz, xz]^T$ is the quadric term calculated from \mathbf{x} , and \mathcal{C}_q , \mathcal{C}_l and c are the coefficients to be fitted. Following Narunas *et al.* [35], we define the cost function for the least-square fitting as the sum of squared differences between the quadric equation and the actual N points:

$$\mathbb{C} \triangleq \sum_{i=1}^N (\mathcal{C}_q \cdot \mathbf{q}_i + \mathcal{C}_l \cdot \mathbf{x}_i - c)^2 \quad (2)$$

The cost function becomes:

$$\mathbb{C} = \sum_{i=1}^N (\mathcal{C}_q \cdot (\mathbf{q}_i - \bar{\mathbf{q}}) + \mathcal{C}_l \cdot (\mathbf{x}_i - \bar{\mathbf{x}}))^2 \quad (3)$$

by setting $\nabla \mathbb{C}_c = 0$ to obtain the optimal c^*

$$c^* = \frac{1}{N} \sum_{i=1}^N (\mathcal{C}_q \cdot \mathbf{q}_i + \mathcal{C}_l \cdot \mathbf{x}_i) \triangleq \mathcal{C}_q \cdot \bar{\mathbf{q}} + \mathcal{C}_l \cdot \bar{\mathbf{x}} \quad (4)$$

where $\bar{\mathbf{q}} = \frac{1}{N} \sum_{i=1}^N \mathbf{q}_i$ are the quadric term averaged on points in a patch, $\bar{\mathbf{x}} = \frac{1}{N} \sum_{i=1}^N \mathbf{x}_i$ is the linear term.

The intermediate variables are defined as follows:

$$\begin{aligned} \mathbb{L} &\triangleq \sum_{i=1}^N (\mathbf{x}_i - \bar{\mathbf{x}}) (\mathbf{x}_i - \bar{\mathbf{x}})^T \\ \mathbb{M} &\triangleq \sum_{i=1}^N (\mathbf{q}_i - \bar{\mathbf{q}}) (\mathbf{q}_i - \bar{\mathbf{q}})^T \\ \mathbb{N} &\triangleq -\sum_{i=1}^N (\mathbf{q}_i - \bar{\mathbf{q}}) (\mathbf{x}_i - \bar{\mathbf{x}})^T \end{aligned} \quad (5)$$

Setting $\nabla \mathbb{C}_{\mathcal{C}_l} = 0$ gives

$$\mathbb{L} \mathcal{C}_l^* = \mathbb{N}^T \mathcal{C}_q \quad (6)$$

By substituting \mathcal{C}_l^* back to Eq. 3, we can obtain

$$\begin{aligned} \mathbb{C} &\triangleq \sum_{i=1}^N \left\| \left((\mathbf{q}_i - \bar{\mathbf{q}})^T + (\mathbf{x}_i - \bar{\mathbf{x}})^T \mathbb{L}^{-1} \mathbb{N}^T \right) \mathcal{C}_q \right\|^2 \\ &= \mathcal{C}_q^T \Psi \mathcal{C}_q, \text{ where } \Psi \triangleq \mathbb{M} - \mathbb{N} \mathbb{L}^{-1} \mathbb{N}^T \end{aligned} \quad (7)$$

Minimizing Eq. 7 over c_q gives the eigenvector c_q^* of Ψ corresponding to the minimum eigenvalue, and c_l^* can be solved from Eq. 6, and c^* from Eq. 4.

As defined by Taubin *et al.* [32], the distance from a point \mathbf{x} to a quadric surface f is:

$$d(\mathbf{x}, f) \approx \frac{f^2(\mathcal{C}, \mathbf{x})}{|\nabla_{\mathbf{x}} f(\mathcal{C}, \mathbf{x})|^2} \quad (8)$$

For every fitted patch, we calculate the average distance between the original points to the fitted surface as the fitting error. Those patches with error exceeding the given threshold will be discarded. We only preserve the patches with relatively small fitting error, which implies a good fitting surface for the following depth correction.

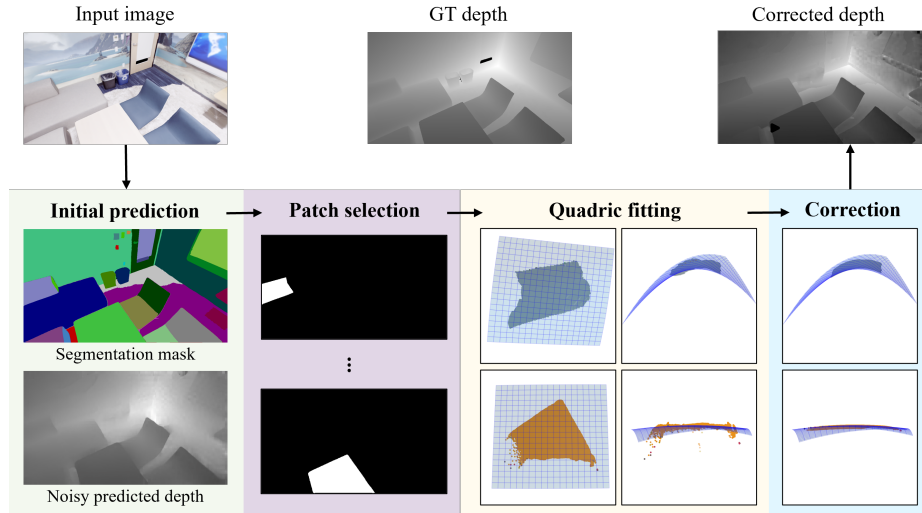


Fig. 3: Quadric-based depth correction. Firstly, segmentation masks are predicted from the input RGB image. Subsequently, the initially noisy predicted depth map undergoes re-projection into 3D space, followed by segmentation into patches. For each patch, a quadric surface is fitted, and the depth value is rectified by recalculating the z coordinate through the quadric function.

Depth correction Through the inverse re-projection using the pixel locations (u, v) and the depth values d , a set of 3D points p can be obtained for each segmented patch, where the depth value directly serves as the z coordinate and K is the calibration matrix:

$$p = \begin{bmatrix} X \\ Y \\ Z \end{bmatrix} = d \cdot \left(K^{-1} \cdot \begin{bmatrix} u \\ v \\ 1 \end{bmatrix} \right) \quad (9)$$

Equipped with the quadric coefficients derived from Section 3.2, we possess the capability to rectify inaccuracies present in the initially noisy depth values. By substituting xy back into $f(\mathcal{C}, \mathbf{x})$, an equation involving z with other variables as constants is obtained. Solving this equation yields new z values, representing the rectified depth values. This enables the storage of corrected values at their original (u, v) positions, thereby avoiding challenges associated with re-projection errors. This approach enhances the precision and reliability of the 3D representation. The established quadric surface model proves effective in mitigating noise impact on depth information, ultimately improving the fidelity of the reconstructed spatial data.

Figure 3 illustrates the effectiveness of our proposed quadratically rectified approach. The original patch exhibits drifting points, particularly along the boundary where significant depth value changes occur. However, the proposed approach rectifies these points, fitting them to the quadric surface. A comparison between the corrected and noisy predicted depth maps clearly shows that the boundaries of different patches become more defined, closely resembling the ground truth depth.

The incorporation of additional constraints imposed by quadric surfaces contributes to a more precise depth prediction, thereby enhancing tracking and mapping accuracy.

3.3 Quadric Ray transformer

Intra-Ray Transformer Drawing inspiration from the ray transformer used in IBRNet [38], our approach employs an attention mechanism along the ray to model relationships between sampled points. Initially, rays are constructed from the provided image and calibration matrix, and N_s points are uniformly sampled along each ray within the range $[d_{near}, d_{far}]$. Utilizing the corrected depth values, denoted as d , we refine the sampling process by selecting additional N_d samples within the range of $[0.95d, 1.05d]$. We do not simply sample around d because potential errors in the corrected depth values might lead to an extended sampling distance away from the true surface.

Following TensoRF [3], we factorize the 4D tensor representing a scene into vectors and matrices. Given the sampled points $p \in R^{B \times (N_s + N_d) \times 3}$, where B is the number of sampled rays, we query the volume density features $f_\sigma \in R^{B \times (N_s + N_d) \times D}$ and feed them into the intra-ray transformer. Processing density features instead of color features is a wise choice as they solely depend on xyz positions, simplifying feature aggregation based on the attention mechanism. Additionally, the smaller number of feature channels in density does not significantly increase the computational burden. The density features of each point along the ray are updated using a self-attention module:

$$f'_\sigma = \text{Attention}(Q(f_\sigma + \delta_p), K(f_\sigma + \delta_p), V(f_\sigma + \delta_p)) \quad (10)$$

where δ_p is the positional encoding in attention mechanism. This self-attention mechanism facilitates feature aggregation along a ray, enabling the capture of more information from the surface and nearby points for more precise surface reconstruction.

Inter-Ray Transformer Intuitively, points belonging to the same semantic quadric are more likely to exhibit similar textural and spatial features, while rays sampled from different quadric surfaces might differ from each other in terms of textures and geometries.

Therefore, leveraging the updated density features obtained from the intra-ray transformer, which incorporates rich spatial information along the ray, we further propose the inter-ray transformer to capture the relationship across rays.

The inter-ray transformer operates on the updated density features of ray points by incorporating the semantic information. First, the updated density features f'_σ are concatenated with the semantic features f_s . Followed by a fusion network, new density features, $f''_\sigma \in R^{B \times N \times D}$, which integrate the semantic priors can be obtained.

$$f''_\sigma = \text{MLP}_{fusion} (f'_\sigma \oplus f_s) \quad (11)$$

As shown in Fig. 4, the inter-ray transformer then takes the transposed density features, $f''^T \in R^{N \times B \times D}$, as input, where the attention map is calculated across different rays along the B dimension:

$$f'''^T = \text{Attention} (Q(f''^T + \delta'_p), K(f''^T + \delta'_p), V(f''^T + \delta'_p)) \quad (12)$$

where δ'_p is the positional encoding in attention mechanism. The inter-ray transformer further facilitates feature interaction across rays. Together with the intra-ray transformer, our proposed network achieves feature aggregation across a broad range of ray points, enhancing rendering accuracy by incorporating quadric priors and additional spatial information.

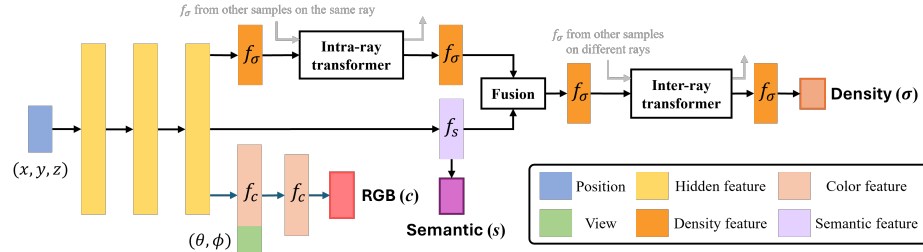


Fig. 4: The detailed structure of quadric ray transformer.

3.4 Joint Optimization of Rendering and Pose Estimation

During mapping, we map the 3D coordinates \mathbf{x} , and viewing directions (θ, ϕ) to volume density, color and semantic logits $(\sigma, \mathbf{c}, \mathbf{s})$. Subsequently, volume rendering is utilized to reconstruct color $\hat{\mathbf{C}}$, depth $\hat{\mathbf{D}}$, and semantic map $\hat{\mathbf{S}}$. For points $\{p_i | i = 1, \dots, M\}$ on a fitted quadric surface, the color and depth loss is calculated as follows:

$$\mathcal{L}_c = \frac{1}{\varepsilon M} \sum_{m=1}^M \left| \mathbf{C}_m - \hat{\mathbf{C}}_m \right|; \mathcal{L}_d = \frac{1}{\varepsilon M} \sum_{m=1}^M \left| \mathbf{D}_m - \hat{\mathbf{D}}_m \right| \quad (13)$$

Here, the fitting error ε functions as an uncertainty penalty. In cases where the fitting is not perfect, the quadric plane is less likely to exhibit similar texture and spatial features, resulting in reduced usefulness of the quadric transformer. Consequently,

such patches are down-weighted by incorporating the fitting error ε . Following Zhi *et al.* [50], we use a multi-class cross-entropy loss as the semantic loss \mathcal{L}_s . Hence the rendering loss is a weighted sum of \mathcal{L}_c , \mathcal{L}_d and \mathcal{L}_s with hyperparameters λ_1 and λ_2 .

$$\mathcal{L} = \mathcal{L}_c + \lambda_1 \mathcal{L}_d + \lambda_2 \mathcal{L}_s \quad (14)$$

For joint optimization, the camera pose $\mathbf{G} = \{g_t\}$, a 4×4 transformation matrix, is converted to quaternion (4×1) and translation (3×1) vector, which are then taken as trainable parameters to the network, optimized together with the NeRF parameters while minimizing the rendering loss. In this way, the camera poses \mathbf{G} and network parameters Θ can be jointly optimized, enhancing both the tracking and mapping accuracy.

4 Experiments

4.1 Experimental Setup

Dataset. Q-SLAM is evaluated on a variety of datasets, including Replica [28], ScanNet [6], and TUM RGB-D [29] dataset. For evaluation of the reconstruction quality, we test our method on 8 synthetic scenes from Replica, which provides high-quality synthetic scenes, akin to the evaluation framework adopted by NeRF-SLAM [22]. Following GO-SLAM [49], we evaluate the tracking accuracy on ScanNet dataset which offers extensively annotated RGB-D scans of real-world scenarios, encompassing challenging short and long trajectories. Following Nice-SLAM [52], we also evaluate on various scenes on indoor TUM RGB-D dataset, with ground truth poses provided by a motion capture system. For camera tracking assessment, our approach is evaluated under two distinct modes: one utilizing ground truth and the other utilizing estimated depth from monocular images as inputs. The input images are resized to 640×320 for Replica dataset, 320×240 for ScanNet dataset and 512×384 for TUM RGB-D dataset.

Metrics. We evaluate tracking accuracy by aligning the estimated trajectory with the ground truth trajectory and computing the Root Mean Square Error (RMSE) of the Absolute Trajectory Error (ATE). In line with NeRF-SLAM [22], we employ the Depth L1 metric to evaluate depth prediction and utilize Peak Signal-to-Noise Ratio (PSNR), SSIM [39], and LPIPS [47] for image rendering evaluation.

Implementation Details. All experimental procedures are executed on an NVIDIA A6000 GPU using PyTorch 1.10.0. We use Adam as the optimizer with $\beta_1 = 0.9$ and $\beta_2 = 0.999$. The tracking module is adapted from Droid-SLAM [34], and pretrained weights are utilized to estimate depths and poses. Our mapping backbone is TensoRF [3], incorporating our proposed depth correction and quadric ray transformer. Diverging from methodologies where scene meshes are reconstructed using marching cubes on Signed Distance Function (SDF) values of queried points, Q-SLAM renders images and depths over the estimated camera trajectory and use TSDF-Fusion [46] for mesh construction with voxel size 1 cm. During the fitting process, only quadric surfaces with fitting error lower than the specified threshold undergo depth correction; otherwise, the uncorrected predicted depth is used for the supervision of NeRF training. For joint

Table 1: Photometric (PSNR [dB], SSIM, LPIPS) and Geomertric (Depth L1 [cm]) results on Replica dataset [28]. Higher PSNR values mean better color rendering performance and lower Depth L1 values denote better depth reconstruction.

Method	Metric	Room0	Room1	Room2	Office0	Office1	Office2	Office3	Office4	Avg.	
Nice-SLAM [52]	PSNR \uparrow	22.12	22.47	24.52	29.07	30.34	19.66	22.23	24.94	24.42	
	SSIM \uparrow	0.63	0.75	0.81	0.87	0.88	0.79	0.85	0.89	0.83	
	(GT depth)	LPIPS \downarrow	0.33	0.27	0.20	0.22	0.18	0.23	0.20	0.19	0.23
	Depth L1 \downarrow	3.53	3.60	3.03	5.56	3.35	4.71	3.84	3.35	3.87	
Vox-Fusion [44]	PSNR \uparrow	22.39	22.36	23.92	27.79	29.83	20.33	23.47	25.21	24.41	
	SSIM \uparrow	0.68	0.75	0.79	0.85	0.87	0.79	0.80	0.84	0.80	
	(GT depth)	LPIPS \downarrow	0.30	0.26	0.23	0.24	0.18	0.24	0.21	0.19	0.23
	Depth L1 \downarrow	2.51	1.69	3.37	2.55	2.08	3.03	2.89	2.86	2.67	
SplaTAM [10]	PSNR \uparrow	32.86	33.89	35.25	38.26	39.17	31.97	29.70	31.81	34.11	
	SSIM \uparrow	0.98	0.97	0.98	0.98	0.98	0.97	0.95	0.95	0.97	
	(GT depth)	LPIPS \downarrow	0.07	0.10	0.08	0.09	0.09	0.10	0.12	0.15	0.10
	Depth L1 \downarrow	0.63	0.62	0.98	0.57	1.66	7.32	3.94	0.88	2.08	
Ours	PSNR \uparrow	33.24	34.81	34.16	39.32	39.51	34.08	32.65	34.93	35.34	
	SSIM \uparrow	0.98	0.99	0.98	0.99	0.99	0.98	0.96	0.98	0.98	
	(GT depth)	LPIPS \downarrow	0.13	0.11	0.11	0.10	0.10	0.13	0.13	0.11	0.12
	Depth L1 \downarrow	0.82	0.77	1.35	1.74	1.56	4.23	3.23	1.26	1.87	
COLMAP [26]	PSNR \uparrow	20.93	11.67	10.35	5.88	5.88	15.66	13.73	17.47	12.70	
	SSIM \uparrow	0.77	0.69	0.75	0.59	0.53	0.80	0.79	0.81	0.72	
	(Predicted depth)	LPIPS \downarrow	0.29	0.44	0.33	0.44	0.33	0.30	0.29	0.27	0.34
	Depth L1 \downarrow	3.87	27.29	5.41	5.21	12.69	4.28	5.29	5.45	8.69	
Droid-SLAM [34]	PSNR \uparrow	18.25	18.65	13.49	16.13	10.31	14.78	15.53	15.71	15.36	
	SSIM \uparrow	0.73	0.79	0.78	0.76	0.65	0.80	0.79	0.80	0.76	
	(Predicted depth)	LPIPS \downarrow	0.35	0.28	0.29	0.29	0.28	0.30	0.30	0.31	0.30
	Depth L1 \downarrow	12.18	8.35	3.26	3.01	2.39	5.66	4.49	4.65	5.50	
Nicer-SLAM [51]	PSNR \uparrow	25.33	23.92	26.12	28.54	25.86	21.95	26.13	25.47	25.41	
	SSIM \uparrow	0.75	0.77	0.83	0.86	0.85	0.82	0.85	0.86	0.82	
	(Predicted depth)	LPIPS \downarrow	0.25	0.21	0.17	0.17	0.17	0.19	0.16	0.17	0.19
	Depth L1 \downarrow	2.53	3.93	3.40	5.49	3.45	4.02	3.34	3.03	3.65	
Ours	PSNR \uparrow	29.58	32.74	31.25	36.31	37.22	30.68	30.21	31.96	32.49	
	SSIM \uparrow	0.83	0.91	0.87	0.94	0.94	0.90	0.88	0.89	0.89	
	(Predicted depth)	LPIPS \downarrow	0.18	0.16	0.15	0.13	0.15	0.20	0.19	0.18	0.17
	Depth L1 \downarrow	1.32	1.19	2.48	3.29	3.07	3.87	4.24	2.78	2.76	

optimization, the scene representation parameters Θ are optimized for 5 steps, and the accumulated losses are then utilized to update camera pose \mathbf{G} .

4.2 Comparison with SOTA

Replica dataset. We evaluate on the 8 scenes as Nice-SLAM and iMAP. As shown in Tab. 1, the results demonstrate comparable performance across almost all scenes in terms of Depth L1 and PSNR metrics. Notably, our approach exhibits performance on par with SLAM systems that utilize ground truth depth for supervision.

TUM-RGBD dataset. We evaluate the tracking performance of our methods on the small-scale indoor-scene dataset with two different inputs, monocular and RGBD images. As presented in Table 2, our approach outperforms traditional SLAM, including ORB-SLAM2 [18] and ORB-SLAM3 [1], which exhibits failures in certain scenarios. In comparison to recent NeRF-based SLAM systems, our solution consistently achieves superior results across most scenes. We attribute the improvements to our

Table 2: ATE RMSE [m] Results on TUM [29] dataset freiburg1 set (monocular setting). ORB-SLAM2 [18] and ORB-SLAM3 [1] fail on certain scenes.

	360	desk	desk2	floor	plant	room	rpy	teddy	xyz	avg
ORB-SLAM2 [18]	-	0.071	-	0.023	-	-	-	-	0.010	-
ORB-SLAM3 [1]	-	0.017	0.210	-	0.034	-	-	-	0.009	-
DeepV2D [33]	0.243	0.166	0.379	1.653	0.203	0.246	0.105	0.316	0.064	0.375
DeepFactors [5]	0.159	0.170	0.253	0.169	0.305	0.364	0.043	0.601	0.035	0.233
DROID-SLAM [34]	0.111	0.018	0.042	0.021	0.016	0.049	0.026	0.048	0.012	0.038
GO-SLAM [49]	0.089	0.016	0.028	0.025	0.026	0.052	0.019	0.048	0.010	0.035
Ours	0.086	0.013	0.023	0.026	0.027	0.049	0.021	0.049	0.009	0.033

proposed quadric representation and quadric transformer, especially for scenes with well-segmented planes and surfaces such as desks, floors, and rooms.

Following GO-SLAM [49], we also test our solution with RGBD images as input, as indicated in Table 3. While the quadric-based depth correction is not performed under this setting, our proposed quadric ray transformer and semantic supervision also contribute to the performance improvement.

Table 3: ATE [m] Results on TUM dataset [29] with RGB-D inputs from freiburg1, freiburg2 and freiburg3 set.

Method	fr1/desk	fr2/xyz	fr3/office
Kintinous [19]	0.037	0.029	0.030
BAD-SLAM [27]	0.017	0.011	0.017
ORB-SLAM2 [18]	0.016	0.004	0.010
iMAP [30]	0.049	0.020	0.058
NICE-SLAM [52]	0.027	0.018	0.030
Ours	0.014	0.005	0.011

Table 4: Comparison of runtime and memory usage. Tested on Replica office0 on NVIDIA A6000 GPU.

Method	Memory Usage	Tracking /frame	Mapping /frame
iMAP [30]	11.72 GB	0.14s	0.32s
Nice-SLAM [52]	10.13 GB	1.32s	10.92s
Vox-Fusion [44]	12.45 GB	0.36s	0.55s
Ours	14.59 GB	0.44s	0.89s

ScanNet dataset. For a comprehensive comparison, we further evaluate our SLAM system on ScanNet [6] dataset, encompassing both long and short sequences. As depicted in Tab. 5, our method outperforms other approaches in both monocular and RGBD setting, with a more pronounced superiority evident in the case of monocular inputs.

Runtime and Memory Usage. In Table 4, we also report the runtime and memory usage on the Replica dataset. The tracking and mapping time is reported per frame. It can be observed that our method can achieve comparable speed with Vox-Fusion [44], but providing much higher rendering quality as shown in Tab 1.

Table 5: ATE RMSE [cm] Results on ScanNet dataset [6]. 'VO' denotes visual odometry. Results of DROID-SLAM are from [49] and results of iMAP* and Nice-SLAM are from [52].

Setting	Scene ID	0000	0054	0233	0465	0059	0106	0169	0181	Avg.
		# Frames	5578	6629	7643	6306	1807	2324	2034	
RGBD	iMAP* [30]	55.95	70.11	86.42	85.03	32.06	17.50	70.51	32.10	56.21
	Nice-SLAM [52]	8.64	20.93	9.00	22.31	12.25	8.09	10.28	12.93	13.05
	DROID-SLAM (VO) [34]	8.00	29.28	6.75	11.37	11.30	9.97	8.64	7.38	11.59
	DROID-SLAM [34]	5.36	8.89	4.90	8.32	7.72	7.06	8.01	6.97	7.15
	GO-SLAM [49]	5.35	8.75	4.78	8.15	7.52	7.03	7.74	6.84	7.02
	Ours	5.23	8.57	4.68	8.33	7.63	7.02	7.66	6.52	6.96
Mono	DROID-SLAM (VO) [34]	11.05	204.31	71.08	117.84	67.26	11.20	16.21	9.94	63.61
	DROID-SLAM [34]	5.48	197.71	72.23	114.36	9.00	6.76	7.86	7.41	52.60
	GO-SLAM [49]	5.94	13.29	5.31	79.51	8.27	8.07	8.42	8.29	17.59
	Ours	5.77	12.62	5.27	76.96	8.46	8.38	8.74	8.76	16.87

4.3 Alation Study

Depth Correction. In Tab. 6 (a), we compare the performance with or without the proposed quadric depth correction module. It can be observed that the depth correction process enhances the accuracy of the predicted depth map by introducing additional surface constraints, rectifying drifting points that deviate from the surfaces. This improvement positively impacts both tracking and mapping performance, especially for the Depth L1 metric.

Table 6: The ablation study of mapping and tracking on Replica dataset office0.

		Depth L1 [cm] ↓ PSNR [dB] ↑	ATE RMSE [cm] ↓
(a)	Ours (w/o quadric depth correction)	5.63	32.55
	Ours (full, with quadric depth correction)	3.29	36.31
(b)	Ours (w/o quadric ray transformer)	5.02	33.13
	Ours (w only intra-ray transformer)	4.36	34.78
	Ours (full, with quadric ray transformer)	3.29	36.31
(c)	Ours (w/o joint optimization)	4.42	34.21
	Ours (full, with joint optimization)	3.29	36.31
(d)	Ours (w/o semantic supervision)	5.87	31.18
	Ours (full, with semantic supervision)	3.29	36.31

Quadric Ray Transformer. In experiments without the quadric ray transformer, the points along a sampled ray are processed independently, lacking feature interaction

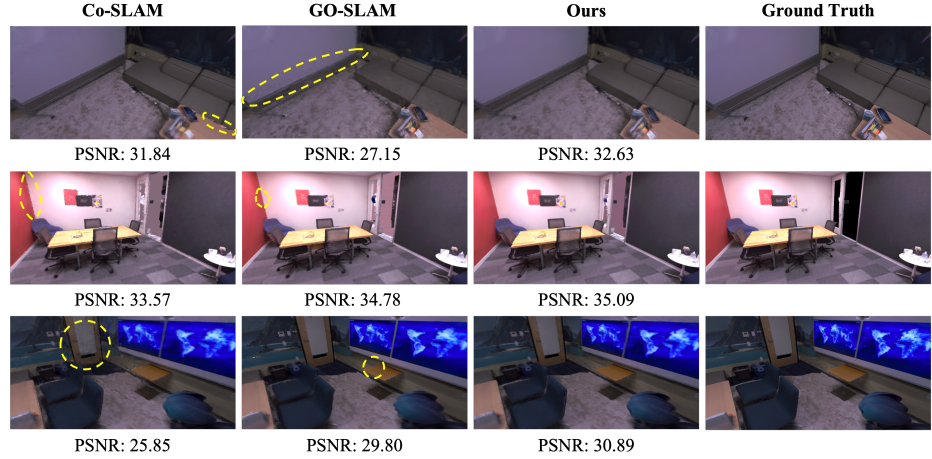


Fig. 5: Qualitative reconstruction results on Replica dataset. We compare our solution with recent SOTA SLAM systems Co-SLAM [36] and GO-SLAM [49]. Our method can recover better texture features, especially on the boundary of instances.

between each other. The introduction of the intra-ray transformer can help capture information along the ray, and hence improve the performance. As illustrated in Tab. 6 (b), the model incorporating both intra-ray and inter-ray transformer exhibits the best performance, and the inclusion of a single intra-ray transformer also contributes to accuracy improvement.

Joint Optimization. For experiments without joint optimization, the estimated camera poses are not optimized using the rendering loss during the mapping process. It can be observed from Tab. 6 (c) that joint optimization of camera poses and 3D reconstruction demonstrates a modest improvement in both tracking and mapping accuracy. We believe that the limited improvement stems from the fact that joint optimization is solely conducted on keyframes during the mapping process. Given that keyframes constitute only a small portion of the entire sequence, while the evaluation of camera poses spans all frames, this potentially constrains the impact of joint optimization.

Semantic Supervision. With an additional semantic head, our model not only renders color and depth but also generates the semantic map. It’s intuitive to utilize segmentation results from previous modules as a supervisory signal, enriching the available information. As shown in Table 6 (d), incorporating semantic supervision can significantly enhance performance.

5 Conclusion

In this paper, we introduce quadratic surfaces as the map representation for SLAM. Based on segmentation results from RGB images, the roughly estimated depth values

can be corrected by incorporating additional surface constraints. We utilize the rectified depths and quadric semantics as a prior for sampling points along the ray, significantly reducing the required number of samples to achieve comparable results, thus alleviating the computational burden. Additionally, we employ a novel quadric-ray transformer model to capture interrelations across different samples along the ray within the constraints of quadric surfaces. Furthermore, we propose an end-to-end joint optimization approach for pose estimation and 3D reconstruction. Sufficient experiments on various datasets demonstrate the effectiveness of our proposed method in terms of novel-view synthesis, depth estimation, and camera tracking.

References

1. Campos, C., Elvira, R., Rodríguez, J.J.G., Montiel, J.M., Tardós, J.D.: Orb-slam3: An accurate open-source library for visual, visual–inertial, and multimap slam. *IEEE Transactions on Robotics* **37**(6), 1874–1890 (2021)
2. Chang, D., Božič, A., Zhang, T., Yan, Q., Chen, Y., Süsstrunk, S., Nießner, M.: Rc-mvsnet: unsupervised multi-view stereo with neural rendering. In: European Conference on Computer Vision. pp. 665–680. Springer (2022)
3. Chen, A., Xu, Z., Geiger, A., Yu, J., Su, H.: Tensorf: Tensorial radiance fields. In: European Conference on Computer Vision. pp. 333–350. Springer (2022)
4. Chen, A., Xu, Z., Zhao, F., Zhang, X., Xiang, F., Yu, J., Su, H.: Mvsnerf: Fast generalizable radiance field reconstruction from multi-view stereo. In: Proceedings of the IEEE/CVF International Conference on Computer Vision. pp. 14124–14133 (2021)
5. Czarnowski, J., Laidlow, T., Clark, R., Davison, A.J.: Deepfactors: Real-time probabilistic dense monocular slam. *IEEE Robotics and Automation Letters* **5**(2), 721–728 (2020)
6. Dai, A., Chang, A.X., Savva, M., Halber, M., Funkhouser, T., Nießner, M.: Scannet: Richly-annotated 3d reconstructions of indoor scenes. In: Proceedings of the IEEE conference on computer vision and pattern recognition. pp. 5828–5839 (2017)
7. Guo, H., Peng, S., Lin, H., Wang, Q., Zhang, G., Bao, H., Zhou, X.: Neural 3d scene reconstruction with the manhattan-world assumption. In: CVPR (2022)
8. Han, X., Yang, L.: Sq-slam: Monocular semantic slam based on superquadric object representation. *Journal of Intelligent & Robotic Systems* **109**(2), 29 (2023)
9. Johari, M.M., Carta, C., Fleuret, F.: Eslam: Efficient dense slam system based on hybrid representation of signed distance fields. In: Proceedings of the IEEE/CVF Conference on Computer Vision and Pattern Recognition. pp. 17408–17419 (2023)
10. Keetha, N., Karhade, J., Jatavallabhula, K.M., Yang, G., Scherer, S., Ramanan, D., Luiten, J.: Splatam: Splat, track & map 3d gaussians for dense rgb-d slam. arXiv preprint arXiv:2312.02126 (2023)
11. Kerbl, B., Kopanas, G., Leimkühler, T., Drettakis, G.: 3d gaussian splatting for real-time radiance field rendering. *ACM Transactions on Graphics* **42**(4) (2023)
12. Li, Z., Wang, Q., Cole, F., Tucker, R., Snavely, N.: Dynibar: Neural dynamic image-based rendering. In: Proceedings of the IEEE/CVF Conference on Computer Vision and Pattern Recognition (CVPR). pp. 4273–4284 (June 2023)
13. Mildenhall, B., Srinivasan, P.P., Tancik, M., Barron, J.T., Ramamoorthi, R., Ng, R.: Nerf: Representing scenes as neural radiance fields for view synthesis. In: ECCV (2020)
14. Mildenhall, B., Srinivasan, P.P., Tancik, M., Barron, J.T., Ramamoorthi, R., Ng, R.: Nerf: Representing scenes as neural radiance fields for view synthesis. *Communications of the ACM* **65**(1), 99–106 (2021)

15. Monnier, T., Austin, J., Kanazawa, A., Efros, A.A., Aubry, M.: Differentiable Blocks World: Qualitative 3D Decomposition by Rendering Primitives. In: NeurIPS (2023)
16. Müller, T., Evans, A., Schied, C., Keller, A.: Instant neural graphics primitives with a multiresolution hash encoding. ACM Transactions on Graphics (ToG) **41**(4), 1–15 (2022)
17. Müller, T., Evans, A., Schied, C., Keller, A.: Instant neural graphics primitives with a multiresolution hash encoding. ACM Trans. Graph. **41**(4), 102:1–102:15 (Jul 2022)
18. Mur-Artal, R., Tardós, J.D.: Orb-slam2: An open-source slam system for monocular, stereo, and rgb-d cameras. IEEE transactions on robotics **33**(5), 1255–1262 (2017)
19. Newcombe, R.A., Izadi, S., Hilliges, O., Molyneaux, D., Kim, D., Davison, A.J., Kohi, P., Shotton, J., Hodges, S., Fitzgibbon, A.: Kinectfusion: Real-time dense surface mapping and tracking. In: 2011 10th IEEE international symposium on mixed and augmented reality. pp. 127–136. Ieee (2011)
20. Nicholson, L., Milford, M., Sünderhauf, N.: Quadricslam: Dual quadrics from object detections as landmarks in object-oriented slam. IEEE Robotics and Automation Letters **4**(1), 1–8 (2018)
21. Park, J., Xu, C., Yang, S., Keutzer, K., Kitani, K.M., Tomizuka, M., Zhan, W.: Time will tell: New outlooks and a baseline for temporal multi-view 3d object detection. In: The Eleventh International Conference on Learning Representations (2023)
22. Rosinol, A., Leonard, J.J., Carbone, L.: Nerf-slam: Real-time dense monocular slam with neural radiance fields. arXiv preprint arXiv:2210.13641 (2022)
23. Rukhovich, D., Vorontsova, A., Konushin, A.: Imvoxelnet: Image to voxels projection for monocular and multi-view general-purpose 3d object detection. In: Proceedings of the IEEE/CVF Winter Conference on Applications of Computer Vision. pp. 2397–2406 (2022)
24. Salas-Moreno, R.F., Glocken, B., Kelly, P.H., Davison, A.J.: Dense planar slam. In: 2014 IEEE international symposium on mixed and augmented reality (ISMAR). pp. 157–164. IEEE (2014)
25. Sandström, E., Li, Y., Van Gool, L., Oswald, M.R.: Point-slam: Dense neural point cloud-based slam. In: Proceedings of the IEEE/CVF International Conference on Computer Vision. pp. 18433–18444 (2023)
26. Schonberger, J.L., Frahm, J.M.: Structure-from-motion revisited. In: Proceedings of the IEEE conference on computer vision and pattern recognition. pp. 4104–4113 (2016)
27. Schops, T., Sattler, T., Pollefeys, M.: Bad slam: Bundle adjusted direct rgb-d slam. In: Proceedings of the IEEE/CVF Conference on Computer Vision and Pattern Recognition. pp. 134–144 (2019)
28. Straub, J., Whelan, T., Ma, L., Chen, Y., Wijmans, E., Green, S., Engel, J.J., Mur-Artal, R., Ren, C., Verma, S., et al.: The replica dataset: A digital replica of indoor spaces. arXiv preprint arXiv:1906.05797 (2019)
29. Sturm, J., Engelhard, N., Endres, F., Burgard, W., Cremers, D.: A benchmark for the evaluation of rgb-d slam systems. In: 2012 IEEE/RSJ international conference on intelligent robots and systems. pp. 573–580. IEEE (2012)
30. Sucar, E., Liu, S., Ortiz, J., Davison, A.J.: imap: Implicit mapping and positioning in real-time. In: Proceedings of the IEEE/CVF International Conference on Computer Vision. pp. 6229–6238 (2021)
31. Taguchi, Y., Jian, Y.D., Ramalingam, S., Feng, C.: Point-plane slam for hand-held 3d sensors. In: 2013 IEEE international conference on robotics and automation. pp. 5182–5189. IEEE (2013)
32. Taubin, G.: Estimation of planar curves, surfaces, and nonplanar space curves defined by implicit equations with applications to edge and range image segmentation. IEEE Transactions on Pattern Analysis & Machine Intelligence **13**(11), 1115–1138 (1991)
33. Teed, Z., Deng, J.: Deepv2d: Video to depth with differentiable structure from motion. arXiv preprint arXiv:1812.04605 (2018)

34. Teed, Z., Deng, J.: Droid-slam: Deep visual slam for monocular, stereo, and rgb-d cameras. *Advances in neural information processing systems* **34**, 16558–16569 (2021)
35. Vaskevicius, N., Pathak, K., Pascanu, R., Birk, A.: Extraction of quadrics from noisy point-clouds using a sensor noise model. In: 2010 IEEE International Conference on Robotics and Automation. pp. 3466–3471. IEEE (2010)
36. Wang, H., Wang, J., Agapito, L.: Co-slam: Joint coordinate and sparse parametric encodings for neural real-time slam. In: Proceedings of the IEEE/CVF Conference on Computer Vision and Pattern Recognition. pp. 13293–13302 (2023)
37. Wang, P., Liu, L., Liu, Y., Theobalt, C., Komura, T., Wang, W.: Neus: Learning neural implicit surfaces by volume rendering for multi-view reconstruction. arXiv preprint arXiv:2106.10689 (2021)
38. Wang, Q., Wang, Z., Genova, K., Srinivasan, P.P., Zhou, H., Barron, J.T., Martin-Brualla, R., Snavely, N., Funkhouser, T.: Ibrnet: Learning multi-view image-based rendering. In: Proceedings of the IEEE/CVF Conference on Computer Vision and Pattern Recognition. pp. 4690–4699 (2021)
39. Wang, Z., Bovik, A.C., Sheikh, H.R., Simoncelli, E.P.: Image quality assessment: from error visibility to structural similarity. *IEEE transactions on image processing* **13**(4), 600–612 (2004)
40. Xia, C., Xu, C., Rim, P., Ding, M., Zheng, N., Keutzer, K., Tomizuka, M., Zhan, W.: Quadric representations for lidar odometry, mapping and localization. *IEEE Robotics and Automation Letters* **8**(8), 5023–5030 (2023)
41. Xu, C., Wu, B., Hou, J., Tsai, S., Li, R., Wang, J., Zhan, W., He, Z., Vajda, P., Keutzer, K., Tomizuka, M.: Nerf-det: Learning geometry-aware volumetric representation for multi-view 3d object detection. In: ICCV (2023)
42. Xu, Q., Xu, Z., Philip, J., Bi, S., Shu, Z., Sunkavalli, K., Neumann, U.: Point-nerf: Point-based neural radiance fields. In: Proceedings of the IEEE/CVF Conference on Computer Vision and Pattern Recognition. pp. 5438–5448 (2022)
43. Yan, C., Qu, D., Wang, D., Xu, D., Wang, Z., Zhao, B., Li, X.: Gs-slam: Dense visual slam with 3d gaussian splatting. arXiv preprint arXiv:2311.11700 (2023)
44. Yang, X., Li, H., Zhai, H., Ming, Y., Liu, Y., Zhang, G.: Vox-fusion: Dense tracking and mapping with voxel-based neural implicit representation. In: 2022 IEEE International Symposium on Mixed and Augmented Reality (ISMAR). pp. 499–507. IEEE (2022)
45. Yunus, R., Li, Y., Tombari, F.: Manhattanslam: Robust planar tracking and mapping leveraging mixture of manhattan frames. In: 2021 IEEE International Conference on Robotics and Automation (ICRA). pp. 6687–6693. IEEE (2021)
46. Zeng, A., Song, S., Nießner, M., Fisher, M., Xiao, J., Funkhouser, T.: 3dmatch: Learning local geometric descriptors from rgb-d reconstructions. In: CVPR (2017)
47. Zhang, R., Isola, P., Efros, A.A., Shechtman, E., Wang, O.: The unreasonable effectiveness of deep features as a perceptual metric. In: Proceedings of the IEEE conference on computer vision and pattern recognition. pp. 586–595 (2018)
48. Zhang, X., Wang, W., Qi, X., Liao, Z., Wei, R.: Point-plane slam using supposed planes for indoor environments. *Sensors* **19**(17), 3795 (2019)
49. Zhang, Y., Tosi, F., Mattoccia, S., Poggi, M.: Go-slam: Global optimization for consistent 3d instant reconstruction. In: Proceedings of the IEEE/CVF International Conference on Computer Vision. pp. 3727–3737 (2023)
50. Zhi, S., Laidlow, T., Leutenegger, S., Davison, A.J.: In-place scene labelling and understanding with implicit scene representation. In: Proceedings of the IEEE/CVF International Conference on Computer Vision. pp. 15838–15847 (2021)
51. Zhu, Z., Peng, S., Larsson, V., Cui, Z., Oswald, M.R., Geiger, A., Pollefeys, M.: Nicer-slam: Neural implicit scene encoding for rgb slam. arXiv preprint arXiv:2302.03594 (2023)

52. Zhu, Z., Peng, S., Larsson, V., Xu, W., Bao, H., Cui, Z., Oswald, M.R., Pollefeys, M.: Nice-slam: Neural implicit scalable encoding for slam. In: Proceedings of the IEEE/CVF Conference on Computer Vision and Pattern Recognition. pp. 12786–12796 (2022)